Probing Type-I 2HDM light Higgs in the top-pair-associated diphoton channel

Yabo Dong,^{1,*} Kun Wang,^{2,†} and Jingya Zhu^{1,‡}

¹School of Physics and Electronics,

Henan University, Kaifeng 475004, China

²College of Science, University of Shanghai for

Science and Technology, Shanghai 200093, China

(Dated: December 6, 2024)

Abstract

In this study, we investigate the Type-I Two-Higgs-Doublet Model (2HDM-I) as a potential explanation for the 95 GeV diphoton excess reported at the LHC and evaluate the feasibility of discovering a 95 GeV Higgs boson at future hadron colliders. By analyzing the dependence of Higgs boson couplings and decay branching ratios on model parameters, we identify regions of parameter space that are consistent with current theoretical and experimental constraints. Our analysis indicates that direct Higgs search data place stringent constraints on the Higgs-mixing angle parameter α , excluding samples within the range $-0.9 \lesssim \alpha \lesssim 1.3$. Subsequent collider simulations focus on the $pp \to t(\to W^+b)\bar{t}(\to W^-\bar{b})h(\to\gamma\gamma)$ process and its relevant backgrounds. These simulations reveal that at the 14 TeV High-Luminosity LHC (HL-LHC), statistical significances of 2σ and 5σ can be achieved at integrated luminosities of 137 fb⁻¹ and 859 fb⁻¹, respectively. Comparable statistical significance can be achieved more efficiently at the 27 TeV High-Energy LHC (HE-LHC) with integrated luminosities of L=69fb⁻¹ and L=430 fb⁻¹, and at the 100 TeV Future Circular Collider (FCC-hh) with L=6.8 fb⁻¹ and L=42 fb⁻¹. However, achieving comprehensive coverage of the parameters with $\alpha+\beta\approx 0$ at the 2σ level via the diphoton channel remains challenging, even with higher collision energies or increased integrated luminosities.

^{*} dongyb@henu.edu.cn

[†] Corresponding author:kwang@usst.edu.cn

[‡] Corresponding author:zhujy@henu.edu.cn

I. INTRODUCTION

The primary goal of the LHC is to search for the Higgs boson and hypothetical particles beyond the Standard Model (BSM). After the decisive discovery of the 125 GeV Higgs boson by the CMS [1] and ATLAS [2] collaborations in 2012, subsequent measurements have confirmed its mass, spin, width, and couplings [3, 4], largely confirming the predictions of the Standard Model (SM). While the SM remains robust under these experimental validations, the absence of new particle discoveries significantly restricts the parameter space of BSM theories. Nevertheless, persistent anomalies and excess signals observed in experiments at LEP, Tevatron, and LHC hint at the presence of new physics, underscoring the importance of continued investigations into BSM theories. These studies are crucial for defining the limits of the SM and guiding future theoretical and experimental efforts.

As early as 2003, the LEP experiment documented a 2.3σ local excess in the $e^+e^- \rightarrow Z(h \rightarrow b\bar{b})$ channel at about 98 GeV [5]. In 2018, the CMS collaboration combined data from 8 TeV (19.7 fb⁻¹) and 13 TeV (35.9 fb⁻¹) runs to report a $h \rightarrow \gamma\gamma$ excess for a mass of 95.3 GeV with the local (global) significance of 2.8σ (1.3 σ), respectively [6]. More recently, in 2023, ATLAS reported a 1.7 σ excess at a mass of 95.4 GeV in the $h \rightarrow \gamma\gamma$ channel [7]. In 2024, CMS reported a local (global) significance of 2.9σ (1.3 σ) for the same mass hypothesis [8]. At the closely related diphoton invariant mass points of 95.4 GeV and 95.3 GeV, both ATLAS and CMS have reported a persistent signal excess. This excess has shown no sign of diminishing over time, strongly suggesting the possible existence of a scalar particle around 95 GeV in the diphoton channel.

The reported 95 GeV excess has attracted considerable theoretical interest as a possible signal of new physics [9–17]. Recent investigations have meticulously examined this phenomenon across various models, focusing on the presence of a light scalar. These models include the simple SM extensions [18–20], the minimal dilaton model [21, 22], the two Higgs doublet model (2HDM) with a singlet extensions [23–27], the next-to-minimal two Higgs doublet model and its extensions [28–31], the Georgi-Machacek model [32–34], the next-to-minimal supersymmetric model [35–45] and its semi-constrained version [46], etc. For the model of these studies, the light scalar is usually singlet-dominated, mixing in part with the doublet Higgs. On the contrary, less attention has been paid to the model with a doublet-dominated scalar.

In this study, we explore the 2HDM, an additional $SU(2)_L$ Higgs doublet extension of the SM that includes a second Higgs doublet [47–52], to give a correlation explanation of the doublet-dominated scalar. The primary rationale for introducing a second Higgs doublet is rooted in the insufficiency of a single doublet to both endow up-type and downtype quarks with mass and to eliminate anomalies inherent in supersymmetry [53]. The theoretical framework of 2HDM predicts a pseudoscalar Higgs boson, a pair of charged Higgs bosons, and two neutral scalar Higgs bosons. The pseudoscalar Higgs or one of the two neutral scalar Higgs can be a candidate to explain the 95 GeV excess in the experiments. Meanwhile, the inclusion of charged Higgs bosons and pseudoscalar in the 2HDM enriches the phenomenological landscape, offering diverse decay modes and branching ratios beyond those in the SM.

However, the 2HDM is particularly affected by experimental constraints due to its potential role in mediating flavor-changing neutral currents (FCNCs). To mitigate these effects, several variants of the 2HDM have been proposed [54, 55], including type-I (2HDM-I), type-II (2HDM-II), lepton-specific (2HDM-LS), and a flipped model (2HDM-Flipped), etc. Specifically, in the 2HDM-I [51, 56–59], a unique characteristic is that only one scalar doublet Φ_2 couple to quarks and leptons. According to its coupling characteristics, 2HDM-I have some interesting features. For example, only 2HDM-I can predict light neutral scalar h and charged scalar H^{\pm} under current theoretical and experimental constraints. Meanwhile, the light H^{\pm} can give an additional contribution to the process of $h \to \gamma \gamma$ through the loop effect, thereby increasing the decay of h to diphoton and impress other decays [60]. Consequently, the light neutral scalar h in 2HDM-I may be an outstanding candidate to explain the 95 GeV diphoton excess and this work primarily explores such phenomenology of 2HDM-I.

Top-pair-associated channel can effectively reduce the SM background from Z boson. This channel is possible, espically after the SM-like Higgs is confirmed in this channel [61, 62]. Therefore, this work focuses on the top-pair-associated diphoton channel. In this research, we explore the parameter space of the 2HDM-I model, evaluating its viability under current constraints to accommodate a 95 GeV light Higgs boson. Following this analysis, we perform Monte Carlo (MC) simulations to predict the feasibility of testing this model in future collider experiments, with a focus on the top-pair-associated diphoton channel.

The organization of this paper is as follows. In Sec. II, we provide a brief overview of

the 2HDM-I model and the relevant theoretical and experimental constraints. In Sec. III, we analyze the relevant phenomenology of the parameter space, compare the results with experimental data, and discuss their implications. In Sec. IV, we conduct collider simulations and analyze the results. In Sec. V, we present our conclusions.

II. THE TWO-HIGGS DOUBLET MODEL

The 2HDM is a widely accepted and straightforward extension of the SM. The most general scalar potential in this model includes 14 additional parameters. Assuming CP conservation in the Higgs sector, it involves two complex doublets, Φ_1 and Φ_2 , each with a hypercharge Y = +1. The scalar potential is given by [47–49]

$$V(\Phi_{1}, \Phi_{2}) = m_{11}^{2} \Phi_{1}^{\dagger} \Phi_{1} + m_{22}^{2} \Phi_{2}^{\dagger} \Phi_{2} - m_{12}^{2} \left(\Phi_{1}^{\dagger} \Phi_{2} + \text{h.c.} \right) + \frac{\lambda_{1}}{2} \left(\Phi_{1}^{\dagger} \Phi_{1} \right)^{2} + \frac{\lambda_{2}}{2} \left(\Phi_{2}^{\dagger} \Phi_{2} \right)^{2} + \lambda_{3} \Phi_{1}^{\dagger} \Phi_{1} \Phi_{2}^{\dagger} \Phi_{2} + \lambda_{4} \Phi_{1}^{\dagger} \Phi_{2} \Phi_{2}^{\dagger} \Phi_{1} + \frac{\lambda_{5}}{2} \left[\left(\Phi_{1}^{\dagger} \Phi_{2} \right)^{2} + \text{h.c.} \right], \quad (1)$$

where m_{11}^2 , m_{12}^2 , m_{22}^2 , and $\lambda_i (i = 1, 2...5)$ are real parameters. The model contains two complex scalar SU(2) doublets, which are defined as

$$\Phi_i = \begin{pmatrix} \phi_i^+ \\ (v_i + \phi_i + i\eta_i) / \sqrt{2} \end{pmatrix}, \quad i = 1, 2.$$
 (2)

where v_i is the vacuum expectation values (VEVs) of Φ_i , with $\sqrt{v_1^2 + v_2^2} \equiv v \approx 246$ GeV.

The free parameters can then be traded for a more physically meaningful set: m_h , m_H , m_A , $m_{H^{\pm}}$, m_{12}^2 , α , and $\tan \beta$. Here, m_h and m_H denote the masses of two neutral scalar Higgs bosons, m_A represents the pseudoscalar Higgs mass, and $m_{H^{\pm}}$ is the mass of the charged Higgs boson. In addition, α denotes the mixing angle of two neutral Higgs, while $\tan \beta$ is defined as the ratio of the VEVs of Φ_2 and Φ_1 , expressed as $\tan \beta \equiv v_2/v_1$. The lighter h and heavier H are orthogonal combinations of ϕ_1 and ϕ_2 and can be given by:

$$h = -\phi_1 \sin \alpha - \phi_2 \cos \alpha \,, \ H = \phi_1 \cos \alpha - \phi_2 \sin \alpha \,. \tag{3}$$

The masses $m_{H^{\pm}}$ and m_A are specified as follows [48]:

$$m_{H^{\pm}} = \sqrt{\frac{m_{12}^2 - (\lambda_4 + \lambda_5)v_1v_2}{v_1v_2}(v_1^2 + v_2^2)}, \quad m_A = \sqrt{\frac{m_{12}^2 - 2\lambda_5v_1v_2}{v_1v_2}(v_1^2 + v_2^2)}. \tag{4}$$

It follows that, under the assumption $m_{H^{\pm}} = m_A$, the parameters λ_4 and λ_5 are equal.

In the 2HDM-I, the Yukawa couplings of the up-type quarks u_R^i , the down-type quarks d_R^i , and the leptons e_R^i are all assumed to couple exclusively to Φ_2 , effectively eliminating all tree-level flavor-changing neutral currents (FCNCs) [54, 55]. Consequently, the Yukawa terms for the 2HDM-I Lagrangian based on the mass-eigenstate can be expressed as [63]

$$\mathcal{L}_{\text{Yukawa}} = -\sum_{f=u,d,\ell} \frac{m_f}{v} \left(\xi_h^f \bar{f} f h + \xi_H^f \bar{f} f H - i \xi_A^f \bar{f} \gamma_5 f A \right)
- \left\{ \frac{\sqrt{2} V_{ud}}{v} \bar{u} \left(m_u \xi_A^u P_L + m_d \xi_A^d P_R \right) dH^+ + \frac{\sqrt{2} m_\ell \xi_A^\ell}{v} \bar{\nu}_L \ell_R H^+ + \text{h.c.} \right\}, \quad (5)$$

where $P_{R,L} = (1 \pm \gamma_5)/2$, $\xi_h^{u,d,\ell} = \cos \alpha/\sin \beta$, $\xi_H^{u,d,\ell} = -\sin \alpha/\sin \beta$, $\xi_A^u = \cot \beta$ and $\xi_h^{d,\ell} = -\cot \beta$. The couplings of Higgs to fermions and bosons in THDM-I are similar to those in SM, except for extra coefficients [64]. Combined with Eq. (5), the couplings of the light and heavy neutral Higgs bosons (h and H) to the vector bosons VV (VV = WW, ZZ) in THDM-I, C_{hVV} and C_{HVV} , can be derived as follows:

$$C_{hVV} = -C_{hVV}^{SM} \times \sin(\alpha + \beta), \ C_{HVV} = C_{HVV}^{SM} \times \cos(\alpha + \beta).$$
 (6)

The couplings of h and H to fermions in THDM-I, C_{hff} and C_{Hff} , can be derived as follows:

$$C_{hff} = C_{hff}^{SM} \times \cos \alpha / \sin \beta$$
, $C_{Hff} = -C_{Hff}^{SM} \times \sin \alpha / \sin \beta$. (7)

The decay width of the light Higgs to $\gamma\gamma$, denoted as $\Gamma(h\to\gamma\gamma)$, is given as [60, 65]

$$\Gamma(h \to \gamma \gamma) = \frac{G_F \alpha^2 m_h^3}{128\sqrt{2}\pi^3} \left| \sum_{f \in \{t,b\}} C_f Q_f^2 N_c A_{1/2}(\tau_f) + C_W A_1(\tau_W) + C_{H^{\pm}} A_0(\tau_{H^{\pm}}) \right|^2. \tag{8}$$

Here, $C_W = C_{hWW}/C_{hWW}^{SM}$ represents the ratio of Higgs to W boson coupling in the 2HDM relative to that of the SM, and $C_f = C_{hff}/C_{hff}^{SM}$ signifies the corresponding ratio for fermion couplings. Furthermore, $C_{H^{\pm}} = -m_W/gm_{H^{\pm}}^2 \times C_{hH^+H^-}$, where $C_{hH^+H^-}$ is the coupling between h and H^{\pm} , the detailed information can be obtained from Ref. [66]. With $\tau_i = m_h^2/(4m_i^2)$ (for $i = f, W, H^{\pm}$) denotes the normalized mass terms, the functions $A_0, A_{1/2}, A_1$ are defined as follows:

$$A_{0}(\tau_{H^{\pm}}) = -[\tau_{H^{\pm}} - f(\tau_{H^{\pm}})]\tau_{H^{\pm}}^{-2},$$

$$A_{1/2}(\tau_{f}) = 2[\tau_{f} + (\tau_{f} - 1)f(\tau_{f})]\tau_{f}^{-2},$$

$$A_{1}(\tau_{W}) = -[2\tau_{W}^{2} + 3\tau_{W} + 3(2\tau_{W} - 1)f(\tau_{W})]\tau_{W}^{-2},$$
(9)

where

$$f(\tau) = \begin{cases} \arcsin^2 \sqrt{\tau} &, \quad \tau \le 1 \\ -\frac{1}{4} \left[\log \frac{1 + \sqrt{1 - \tau^{-1}}}{1 - \sqrt{1 - \tau^{-1}}} - i\pi \right]^2 &, \quad \tau > 1 \end{cases}$$
 (10)

III. RESULTS OF THEORETICAL AND EXPERIMENTAL CONSTRAINTS

We use the Mathematica package SARAH-4.15.2 [67–70] to generate the model file and then use the package SPheno-4.0.5 [71, 72] to calculate the particle spectrum. The seven input parameters are m_h , m_H , m_A , $m_{H^{\pm}}$, m_{12}^2 , α , and $\tan \beta$. Since one of the CP-even Higgs bosons should be the SM-like, we denote H as the SM-like Higgs with $m_H = 125$ GeV. The mass of h is set to 95 GeV. The other parameters are explored within the following ranges:

$$\alpha \in [-\pi/2, \pi/2],$$

$$\tan \beta \in [0, 20],$$

$$m_{12} \in [-10 \text{ TeV}, 10 \text{ TeV}],$$

$$m_{H^{\pm}} = m_A \in [150 \text{ GeV}, 1000 \text{ GeV}].$$
(11)

For the experimental constraints, we consider the following:

• Constraints from B physics, $B_d \to \mu^+ \mu^-$, $B_s \to \mu^+ \mu^-$ and $B \to X_s \gamma$ [73–77]:

BR(
$$B_d \to \mu^+ \mu^-$$
) $< 2.1 \times 10^{-10}$,
BR($B_s \to \mu^+ \mu^-$) $= (2.9 \pm 0.8) \times 10^{-9}$, (12)
BR($B \to X_s \gamma$) $= (3.32 \pm 0.3) \times 10^{-4}$.

We use the package Superlso-v4.1 [78, 79] to calculate the decay branching ratios in B physics.

• Constraints from muon anomalous magnetic moment at 2σ level [80, 81]

$$\Delta a_{\mu} = (24.9 \pm 4.8) \times 10^{-10}.\tag{13}$$

We calculate the Δa_{μ} with the package GM2Calc-2.2.0 [82, 83] at two-loop level.

• Constraints from direct Higgs searches at LEP, Tevatron, and LHC with the HiggsBounds-5.10.0 package [84], while the Higgs signal strengths with the HiggsSignal-2.6.0 [85].

• Constraints from electroweak precision observables [86, 87] requiring that the oblique parameters S, T, and U to matching the global fit results as detailed in [77]:

$$S = -0.04 \pm 0.10$$
, $T = 0.01 \pm 0.12$, $U = -0.01 \pm 0.09$, (14)

where the correlation coefficients are given as $\rho_{ST}=0.92,\ \rho_{SU}=-0.80,\ {\rm and}\ \rho_{TU}=-0.93.$

For theoretical constraints, we account for the following:

• Constraints from unitarity on scalar parameters requiring that the scalar couplings λ_i (where i = 1, 2, ..., 5) to satisfy specific conditions [88–90]:

$$\begin{vmatrix}
2\lambda_{3} + \frac{\lambda_{5}}{2} &| \leq 8\pi, & | 2\lambda_{3} \pm \lambda_{4} - \frac{\lambda_{5}}{2} &| \leq 8\pi, & | 2\lambda_{3} + \lambda_{4} - \frac{\lambda_{5}}{2} &| \leq 8\pi, \\
|2\lambda_{3} - \lambda_{4} - \frac{5\lambda_{5}}{2} &| \leq 8\pi, & | 2\lambda_{3} + 2\lambda_{4} - \frac{\lambda_{5}}{2} &| \leq 8\pi, \\
|\lambda_{1} + \lambda_{2} + 2\lambda_{3} \pm \sqrt{(\lambda_{1} - \lambda_{2})^{2} + \frac{1}{4}\lambda_{5}^{2}} &| \leq 8\pi, \\
|\lambda_{1} + \lambda_{2} + 2\lambda_{3} \pm \sqrt{(\lambda_{1} - \lambda_{2})^{2} + \frac{1}{4}(-2\lambda_{4} + \lambda_{5})^{2}} &| \leq 8\pi, \\
|3(\lambda_{1} + \lambda_{2} + 2\lambda_{3}) \pm \sqrt{9(\lambda_{1} - \lambda_{2})^{2} + \left(4\lambda_{3} + \lambda_{4} + \frac{1}{2}\lambda_{5}\right)^{2}} &| \leq 8\pi.
\end{vmatrix}$$
(15)

• Constraints from vacuum stability, as outlined in [91]:

$$\lambda_1, \lambda_2 > 0, \ \lambda_3 > -\sqrt{\lambda_1 \lambda_2}, \ \lambda_3 + \min[0, \lambda_4 - |\lambda_5|] > -\sqrt{\lambda_1 \lambda_2}.$$
 (16)

• Constraints from perturbativity, as outlined in [48], requiring that the absolute values of the scalar couplings λ_i (for i = 1, 2, ..., 5) to be less than 8π , specifically, $|\lambda_i| < 8\pi$.

In Fig. 1, we show the surviving samples on the $\tan \beta$ versus α planes (upper panels) and the $|m_{12}|$ versus m_A planes (lower panels), with colors indicating the ratio of χ^2 to the number of observables (n_{obs}) in the left, the branching ratio of $B \to X_s \gamma$ in the middle, and the muon anomalous magnetic moment Δa_{μ} in the right. The light gray samples are excluded based on Higgs direct search data, primarily due to the strong coupling of h to fermions when $\cos \alpha$ is large and $\sin \alpha$ is small. The light blue samples are excluded for

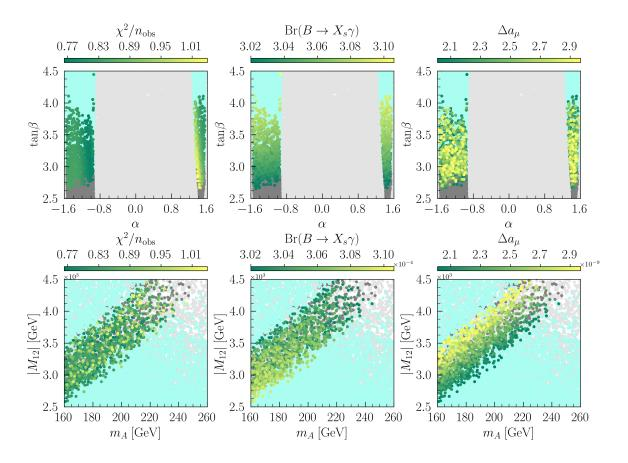


FIG. 1. The surviving samples are shown in the $\tan \beta$ versus α (upper panels) and $|m_{12}|$ versus m_A planes (lower panels), with colors indicating the ratio of χ^2 to the number of observables $(n_{\rm obs})$ (left), the branching ratio $Br(B \to X_s \gamma)$ (middle), and the muon anomalous magnetic moment Δa_{μ} (right). The light gray samples are excluded by direct Higgs searches, the light blue samples are excluded for failing to provide an appropriate muon anomalous magnetic moment, and the gray samples are excluded based on $Br(B \to X_s \gamma)$ data.

failing to provide an appropriate muon anomalous magnetic moment, and the gray samples are excluded based on $Br(B \to X_s \gamma)$ data. One can draw several conclusions from these figures:

• From the left two panels of Fig.1, it is evident that the value of $\chi^2/n_{\rm obs}$ is primarily influenced by α and $\tan \beta$ and is largely insensitive to the values of $|M_{12}|$ and m_A . This is because $\chi^2/n_{\rm obs}$ predominantly evaluates the Higgs signal strength, which is directly linked to its coupling strength. The coupling strength of the Higgs is, in turn, primarily determined by the values of α and $\tan \beta$.

- From the middle two panels of Fig.1, the branching ratio $Br(B \to X_s \gamma)$ is observed to be heavily dependent on $\tan \beta$ and nearly proportional to it. Consequently, lower values of $\tan \beta$ ($\lesssim 2.5$) are excluded, as they fail to produce a sufficient $Br(B \to X_s \gamma)$. Additionally, smaller values of m_A and $|m_{12}|$ are associated with higher $Br(B \to X_s \gamma)$.
- From the right two panels of Fig.1, it is evident that moderate values of $\tan \beta$ (2.5 $\lesssim \tan \beta \lesssim 4$) yield appropriate Δa_{μ} . Larger values of $\tan \beta$ are excluded as they fail to make a sufficiently significant contribution to Δa_{μ} . Furthermore, larger values of $|m_{12}|$ provide significant contributions to Δa_{μ} , resulting in the exclusion of samples with either excessively small ($|m_{12}| \lesssim 20 \, m_A 500 \, \text{GeV}$) or excessively large ($|m_{12}| \gtrsim 20 \, m_A + 500 \, \text{GeV}$) values of $|m_{12}|$ based on muon anomalous magnetic moment data.
- From the right four panels of Fig.1, it is evident that achieving a larger value of $Br(B \to X_s \gamma)$ requires a larger $\tan \beta$ and a smaller $|m_{12}|$. However, these conditions are constrained by muon anomalous magnetic moment data. Consequently, it is challenging to simultaneously achieve both a suitable Δa_{μ} and a large $Br(B \to X_s \gamma)$.
- From the lower right panel of Fig.1, it is evident that larger $|m_{12}|$ contributes positively to Δa_{μ} , whereas larger m_A contributes negatively. This effect arises from additional corrections to the pseudoscalar A induced by one-loop diagrams [92–95], which are expressed as

$$\Delta a_{\mu}^{1L} = \frac{m_{\mu} m_{\tau} \rho^2}{8\pi^2} \left[\frac{\left(\log \frac{m_H^2}{m_{\tau}^2} - \frac{3}{2}\right)}{m_H^2} - \frac{\log \left(\frac{m_A^2}{m_{\tau}^2} - \frac{3}{2}\right)}{m_A^2} \right], \tag{17}$$

where ρ is the coupling parameter for μ and τ to H and A. It can be seen that Δa_{μ} gets a positive contribution at the one-loop level only if m_A is greater than m_H . In our calculations, m_A is not significantly larger than m_H , so the term inside the square brackets is about 10^{-4} , and the term before the square brackets is about 10^{-8} . Consequently, the net contribution from one-loop processes is about 10^{-12} . The two-loop contributions to Δa_{μ} are divided into bosonic (a_{μ}^B) and fermionic (a_{μ}^F) parts, as detailed in [96–98], which given by

$$\Delta a_{\mu}^{\rm 2L} = a_{\mu}^{\rm B} + a_{\mu}^{\rm F} \,.$$
 (18)

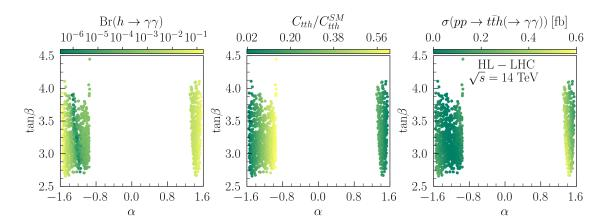


FIG. 2. The surviving samples are shown in the $\tan \beta$ versus α plane, with the color indicating the branching ratio $Br(h \to \gamma \gamma)$ (left), the reduced top-Higgs coupling C_{tth}/C_{tth}^{SM} (normalized to the SM values for the 2HDM-I) (middle), and the cross section $\sigma(pp \to t\bar{t}h(\to \gamma \gamma))$ (right).

The dominant contribution to Δa_{μ} comes from $a_{\mu}^{\rm B}$, which consists of three parts and have

$$a_{\mu}^{\rm B} = a_{\mu}^{\rm EW} + a_{\mu}^{\rm Yuk} + a_{\mu}^{\rm non-Yuk}.$$
 (19)

The components of $a_{\mu}^{\rm B}$ include $a_{\mu}^{\rm EW}$, which corresponds to contributions from the SM-like Higgs, $a_{\mu}^{\rm non-Yuk}$ represents QCD contributions without new Yukawa couplings, and $a_{\mu}^{\rm Yuk}$, which accounts for QCD contributions with new Yukawa couplings. The latter has the form

$$a_{\mu}^{\text{Yuk}} = \frac{\alpha_{em}^2 m_{\mu}^2}{574\pi^2 c_W^4 s_W^4 m_Z^4} \left[a_{0,0}^0 + a_{5,0}^0 \Lambda_5 + \left(a_{0,0}^1 \frac{\tan^2 \beta - 1}{\tan \beta} + a_{5,0}^1 \frac{\tan^2 \beta - 1}{\tan \beta} \Lambda_5 \right) \cos(\beta - \alpha) \right], \tag{20}$$

where Λ_5 is defined as $2m_{12}^2/v^2\sin\beta\cos\beta$, and the coefficients $a_{0,0}^0$, $a_{0,0}^1$, $a_{5,0}^0$, and $a_{5,0}^1$ are given in the Appendix of Ref. [96]. In our analysis, m_{12}^2 is significantly larger than both $\tan\beta$ and v^2 , causing a_{μ}^{Yuk} to be nearly proportional to m_{12}^2 . Consequently, Δa_{μ} increases with increasing m_{12}^2 .

In Fig. 2, we present the surviving samples on the $\tan \beta$ versus α plane, with color indicating the branching ratio $Br(h \to \gamma \gamma)$ in the left, then the reduced top-Higgs coupling C_{tth}/C_{tth}^{SM} (normalized to the SM values for the 2HDM-I) in the middle, and the cross section $\sigma(pp \to t\bar{t}h(\to \gamma \gamma))$ in the right. The formula to calculate the cross section $\sigma(pp \to t\bar{t}h(\to \gamma \gamma))$

 $\gamma\gamma)$) is

$$\sigma(pp \to t\bar{t}(h \to \gamma\gamma)) = |\sigma(pp \to t\bar{t}H)|_{m_h = 95 \text{GeV}}^{SM} \times (C_{t\bar{t}h}/C_{t\bar{t}h}^{SM})^2 \times Br(h \to \gamma\gamma), \tag{21}$$

where $|\sigma(pp \to t\bar{t}H)|_{m_h=95 \text{GeV}}^{SM}$ is the SM cross section for the process $pp \to t\bar{t}H$ with a Higgs mass of 95 GeV. The value at next-to-leading order (NLO) is reported to be 1268 fb, as detailed in Ref. [99]. We can draw several conclusions from these figures:

- From the left panel of Fig.2, it is evident that the branching ratio $Br(h \to \gamma \gamma)$ primarily depends on $\cos \alpha$ and $\tan \beta$. $Br(h \to \gamma \gamma)$ reaches its maximum near $\cos \alpha \approx 0$ and its minimum when $\alpha + \beta \approx 0$. This is because, with $A_0(\tau_{H^{\pm}}) \approx 0.34$, $A_{1/2}(\tau_f) \approx 1.4$, and $A_1(\tau_W) \approx -7.6$, the dominant contributions to $\Gamma(h \to \gamma \gamma)$ originate from W. When $\alpha + \beta \approx 0$, $\sin(\alpha + \beta)$ approaches zero, leading to a negligible decay rate of the Higgs boson into two photons in this region. This observation is consistent with Eq. (6) and Eq. (8).
- In the middle panel of Fig. 2, the ratio C_{tth}/C_{tth}^{SM} appears almost proportional to the value of $\cos \alpha$ and is largely unaffected by $\tan \beta$. This observation is consistent with Eq. (7), which indicates that variations in $\tan \beta$ have minimal impact on $\sin \beta$ when $\tan \beta$ is not too small.
- The right panel shows that the cross section $\sigma(pp \to t\bar{t}h(\to \gamma\gamma))$ reaches its peak, about 0.6 fb, when $\cos \alpha$ is close to 1 and $\tan \beta$ is close to 2.7. This peak arises because both $Br(h \to \gamma\gamma)$ and C_{tth}/C_{tth}^{SM} reaching significant values in this parameter space. The distribution of minimum values mirrors that of $Br(h \to \gamma\gamma)$, because variations in α impact $Br(h \to \gamma\gamma)$ by over five orders of magnitude, whereas C_{tth}/C_{tth}^{SM} changes by only one order of magnitude. Detailed information on the benchmark points is provided in Table I.

IV. FUTURE COLLIDER SIMULATIONS AND DISCUSSION

A. 14 TeV HL-LHC Simulation Result

We focus on the process $pp \to t (\to W^+ b) \bar{t} (\to W^- \bar{b}) h (\to \gamma \gamma)$ at the 14 TeV High Luminosity Large Hadron Collider (HL-LHC) with an integrated luminosity of $L=3~{\rm ab}^{-1}$.

TABLE I. Five benchmark points for surviving samples.

	P1	P2	Р3	P4	P5
$\alpha \; [{\rm GeV}]$	1.40	-1.53	1.44	1.37	1.39
$\tan\!\beta [{\rm GeV}]$	2.78	2.79	2.82	3.08	2.85
$m_{H^\pm}(m_A)~[{ m GeV}]$	213	212	199	197	208
$m_{12} \; [{ m GeV}]$	4254	3765	3870	3637	4250
λ_1	1.51	1.42	1.48	1.77	1.61
λ_2	0.159	0.158	0.157	0.151	0.157
λ_3	1.65	1.70	1.46	1.42	1.59
λ_4	-0.966	-0.942	-0.855	-0.847	-0.937
λ_5	-0.966	-0.942	-0.855	-0.847	-0.937
$T [\times 10^{-2}]$	-1.3	-1.6	-1.4	-1.3	-1.3
$S \left[\times 10^{-3} \right]$	4.3	7.5	6.0	5.4	4.8
$U [\times 10^{-4}]$	-4.2	-5.6	-4.2	-3.9	-4.2
$Br(h \to \gamma \gamma) \ [\%]$	1.3	12	1.8	0.94	1.2
C_{htt}/C_{htt}^{SM}	0.18	0.036	0.14	0.20	0.18
$\sigma(pp \to t\bar{t}h(\to \gamma\gamma)) \ [\text{ fb}^{-1}]$	0.55	0.19	0.45	0.50	0.52
$\chi^2/n_{ m obs}$	1.07	0.88	0.99	1.09	1.05
$Br(B \to X_s \gamma) \ [\times 10^{-4}]$	3.02	3.03	3.02	3.04	3.03
$Br(B_d \to \mu^+ \mu^-) \ [\times 10^{-10}]$	1.0	1.0	1.01	0.99	1.0
$Br(B_s \to \mu^+ \mu^-) \ [\times 10^{-9}]$	3.16	3.16	3.16	3.13	3.15
$\Delta a_{\mu} \ [\times 10^{-9}]$	2.79	2.18	2.56	2.43	2.94

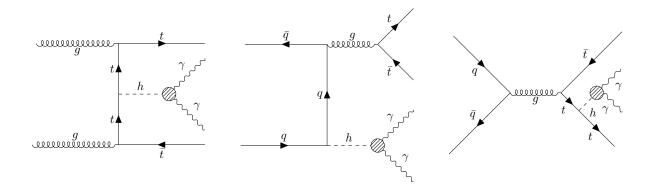


FIG. 3. Main Feynman Diagrams for the Process $pp \to t\bar{t}h(\to \gamma\gamma)$ at Leading Order (LO) in 2HDM-I.

The main leading order (LO) Feynman diagrams for this process in 2HDM-I are shown in Fig. 3. Accompanied by the top quark pair, the h signal decaying into diphoton is more easily distinguished from the SM background due to the unique properties of this channel. One of the most important SM backgrounds is from the Z boson. It has a mass comparable to h, can decay to diphoton, and can be produced directly at tree level at the LHC. Instead, h can only be generated via the loop effect. This will cause the cross section of $pp \to Z$ to be much larger than the cross section of $pp \to h$. Specifically, in scenarios where it is not accompanied by top quark pair production, the cross section for the process $pp \to Z$ can reach up to 4.566×10^4 pb at a center-of-mass energy of 14 TeV, which calculated using the MadGraph5_aMC@NLO_v3.4.2 package [100, 101]. On the contrary, the cross section of $pp \to h$ is only about dozens pb. However, when considering top quark pair production alongside this process, the cross section for $pp \to t\bar{t}Z$ decreases sharply to 0.71 pb. Additionally, since the branching ratio for $Z \to \gamma \gamma$ is less than 1.46×10^{-5} [81], we can conclude that the background from $t\bar{t}Z$ can be effectively neglected in this context.

Due to the decay of h into diphoton, the signal can produce a narrow diphoton resonance, with the resonance peak likely to occur near its mass m_h . Consequently, we categorize the SM backgrounds into resonant and non-resonant types. The resonant category includes $t\bar{t}H$ and tjH, where the SM-like H can decay into diphoton, thereby generating a similar resonance peak. For non-resonant backgrounds, we consider processes such as $t\bar{t}\gamma\gamma$, $b\bar{b}\gamma\gamma$, $tj\gamma\gamma$, $t\bar{t}\gamma$, and $Wjj\gamma\gamma$, where j can be misidentified as a b-jet.

We use the MadGraph5_aMC@NLO_v3.4.2 package [100, 101] for Monte Carlo simulations of the signal and backgrounds. In our simulations, the parton distribution functions (PDFs) are set to NNPDF23LO1 via LHAPDF6 [102, 103]. Particle decay, parton shower, and hadronization processes are simulated using PYTHIA_v8.2 [104] with the MG5a-MC_PY8_interface. Jet clustering is performed using the anti-kT algorithm [105]. Detector effects are simulated using Delphes-3.5.0. [106, 107]. Finally, the event analysis is done with MadAnalysis5 v1.9.60 [108].

In Fig. 4, the normalized distributions of various kinematic variables for the signal and SM background are displayed. In each case, γ_1 denotes the photon with the highest energy, γ_2 the next highest, and similarly for j_1 and j_2 . As expected, both the resonant background and the signal exhibit narrow peaks near their respective Higgs masses in the diphoton invariant mass $M[\gamma_1\gamma_2]$, visible in the lower middle panel of Fig. 4. Their transverse masses $M_T[\gamma_1\gamma_2]$

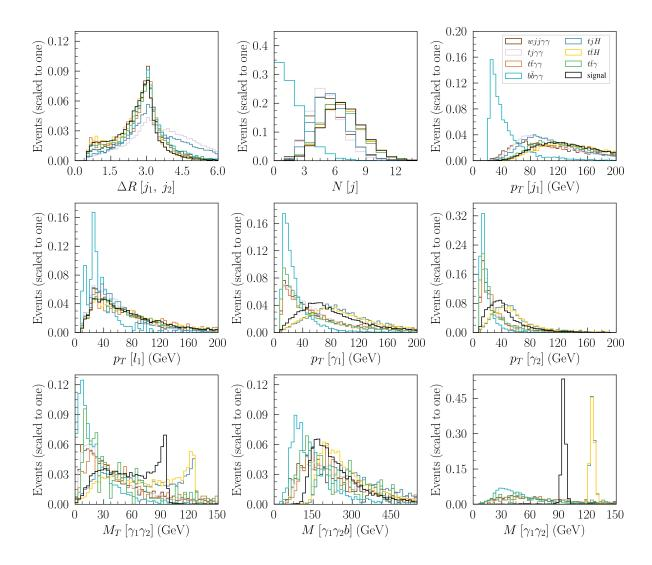


FIG. 4. The normalized distributions of $\Delta R[j_1, j_2]$ (upper left), N[j] (upper middle), $p_T^{j_1}$ (upper right), $p_T^{l_1}$ (upper middle), $p_T^{\gamma_1}$ (middle), $p_T^{\gamma_2}$ (middle right), $M_T[\gamma_1\gamma_2]$ (lower left), $M[\gamma_1\gamma_2]$ (lower middle) and $M[\gamma_1\gamma_2b]$ (lower right).

are truncated near these masses. However, the non-resonant backgrounds tend to have smaller values of $M[\gamma_1\gamma_2]$ and $M_T[\gamma_1\gamma_2]$, making these measures effective for distinguishing between resonant signals, resonant backgrounds, and non-resonant backgrounds. From this figure, we can notice the following details:

• From the upper left panel of Fig. 4, one can see that the backgrounds of tjH and $tj\gamma\gamma$ have more events clustered at larger $\Delta R[j_1, j_2]$ values compared to the signal. Thus, choosing an appropriate $\Delta R[j_1, j_2]$ can effectively reduce these backgrounds.

- The upper middle panel of Fig. 4 shows that the $b\bar{b}\gamma\gamma$ background typically has fewer jets than others. By choosing a higher jet count threshold, N[j], one can significantly reduce this background.
- The upper right, middle and middle right panels of Fig. 4 show that the non-resonant backgrounds, especially $b\bar{b}\gamma\gamma$, typically have lower transverse momenta for j_1 , γ_1 , and γ_2 . Consequently, choosing higher transverse momentum thresholds for these particles can effectively suppress the non-resonant background.
- From the middle panel of Fig. 4, one can observe that both the resonant background and the signal show a preference for a larger invariant mass of γ_1 , γ_2 , and b. Consequently, choosing a higher $M[\gamma_1\gamma_2b]$ can effectively reduce the non-resonant background.

For all events, one of the W bosons must decay into a lepton and a neutrino to suppress the QCD background $b\bar{b}\gamma\gamma$. In such cases, the presence of a lepton along with missing transverse energy ($\not\!E$) will be detectable in the event. To effectively distinguish these events from the background, the leptons, jets, and photons within the events must meet the following criteria:

$$p_T^{j/b} > 20 \text{ GeV}, \ p_T^{\ell/\gamma} > 10 \text{ GeV}, \ |\eta_i| < 5, \ \Delta R[i, j] > 0.4. \ (i, j = j, b, \ell, \gamma)$$
 (22)

In conjunction with Fig. 4, we implement a series of cuts as follows:

• Basic Cut: We select events containing at least one lepton $(N(\ell) \ge 1)$, two photons $(N(\gamma) \ge 2)$, two jets $(N(j) \ge 2)$, and at least one b-jet $(N(b) \ge 1)$. For the transverse momentum (p_T) of jets and photons, the following requirements apply:

$$p_T[\gamma_1] > 30 \text{ GeV}, \ p_T[j_1] > 40 \text{ GeV}, \ p_T[j_2] < 220 \text{ GeV}.$$
 (23)

The spatial separation between jets and photons must satisfy the following criteria:

$$\Delta R[j_1, j_2] < 4, \ \Delta R[\gamma_1, \gamma_2] < 3.6.$$
 (24)

To further suppress the background from $t\bar{t}\gamma$, we require that the phase angle of the b-jet (θ_{b_1}) , the pseudorapidity of the jet and lepton $(\eta_{j_1} \text{ and } \eta_{\ell_1})$, and the Lorentz factor of the jet (γ_{j_1}) meet the following conditions:

$$0.2 < \theta_{b_1} < 3, \ \eta_{j_1} > -2.6, \ \eta_{\ell_1} > -2.5, \ \gamma_{j_1} < 50.$$
 (25)

TABLE II. Cut flow of cross sections at the 14 TeV HL-LHC for benchmark point P1 with an integrated luminosity of L = 300 fb⁻¹, as detailed in Table I.

Cuts	$\operatorname{Signal}(\sigma \times L)$	$\operatorname{Background}(\sigma \times L)$						
	t ar t h	$tar{t}\gamma$	$t ar{t} H$	tjH	$bar{b}\gamma\gamma$	$t \bar t \gamma \gamma$	$tj\gamma\gamma$	$Wjj\gamma\gamma$
Initial	165	1536000	168	23	2293800	3354	5253	65400
Basic cut	14.5	4577.3	17.25	0.712	848.7	200.0	89.61	268.1
Mass cut	11.03	46.08	0.023	0.0	0.0	6.47	2.67	4.58
Energy cut	10.33	0.0	0.023	0.0	0.0	5.8	1.91	3.27

• Mass Cut: For the invariant masses of the diphoton pair $(M[\gamma_1\gamma_2])$ and the photon with jet $(M[\gamma_2j_1])$, we choose:

92 GeV
$$< M[\gamma_1 \gamma_2] < 98$$
 GeV, $M[\gamma_2 j_1] < 390$ GeV. (26)

For the transverse masses of the photon, diphoton, and diphoton with a b-jet $(M_T[\gamma_1], M_T[\gamma_1\gamma_2], \text{ and } M_T[\gamma_1\gamma_2b_1])$, we select:

$$M_T[\gamma_1] < 300 \text{ GeV}, \ M_T[\gamma_1 \gamma_2] < 96 \text{ GeV}, \ M_T[\gamma_1 \gamma_2 b_1] < 440 \text{ GeV}.$$
 (27)

• Energy Cut: The transverse energy (E_T) , transverse hadronic energy (H_T) , missing transverse energy (E_T) , and missing transverse hadronic energy (E_T) must meet the following criteria:

$$E_T > 200 \; {\rm GeV}, \; H_T < 900 \; {\rm GeV}, \; 10 {\rm GeV} < E_T < 190 \; {\rm GeV}, \; E_T > 30 \; {\rm GeV}. \eqno(28)$$

These cuts are performed on both our reference points and background events to calculate the signal significance. The results of these sequential cuts are detailed in Table II, where the integrated luminosity is set to 300 fb⁻¹. The dominant backgrounds, $Wjj\gamma\gamma$, $b\bar{b}\gamma\gamma$, and $t\bar{t}\gamma$, are significantly reduced by more than two to three orders of magnitude after the base cut, while the signal reduction is limited to one order of magnitude. Subsequent cuts at the invariant mass and transverse mass effectively preserved the signal while further reducing the background. After these cuts, $t\bar{t}\gamma$, $t\bar{t}\gamma\gamma$, $tj\gamma\gamma$, and $Wjj\gamma\gamma$ showed reductions of more than an order of magnitude, while $t\bar{t}H$, tjH, and $b\bar{b}\gamma\gamma$ were nearly eliminated. The final cut on transverse energy and transverse hadronic energy additionally minimized the $t\bar{t}\gamma$

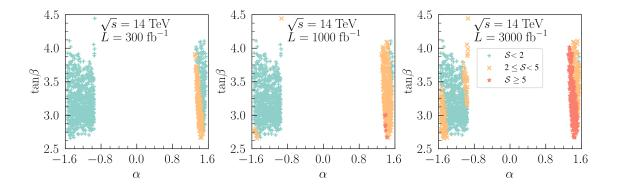


FIG. 5. Statistical Significance of surviving samples in the tan β versus α planes at integrated luminosities of $L = 300 \text{ fb}^{-1}$ (left), $L = 1000 \text{ fb}^{-1}$ (middle), and $L = 3000 \text{ fb}^{-1}$ (right).

background to negligible levels. In the end, only minimal instances of $t\bar{t}H$, $t\bar{t}\gamma\gamma$, $tj\gamma\gamma$, and $Wjj\gamma\gamma$ remained.

Statistical significance was calculated using the Poisson formula [109]

$$S = \sqrt{2L[(S+B)\ln(1+S/B) - S]},$$
(29)

where S and B are the signal and background cross sections, respectively, and L is the integrated luminosity. For the benchmark point P1 from Table I and an integrated luminosity of L = 300 fb⁻¹, the statistical significance achieves 2.8σ .

In Fig. 5, The statistical significance of other surviving points at luminosities of L = 300 fb⁻¹ (left), L = 1000 fb⁻¹ (middle), and L = 3000 fb⁻¹ (right) are displayed. We can draw the following conclusions from these figures:

- For the HL-LHC, to get a significance of 2σ or 5σ , requires at least about $L=137~{\rm fb}^{-1}$ or $L=859~{\rm fb}^{-1}$.
- The left panel of Fig. 5 shows that some surviving samples reach the 2σ level at $L = 300 \, \text{fb}^{-1}$ if and only if $\alpha > 0$.
- The middle panel of Fig. 5 shows that few surviving samples reach the 5σ level around $\alpha \approx 1.5$ for $L = 1000~{\rm fb}^{-1}$.
- The right panel of Fig. 5 shows that all samples can be covered at 2σ or 5σ levels for $L = 3000 \text{ fb}^{-1}$ when $\alpha > 0$.

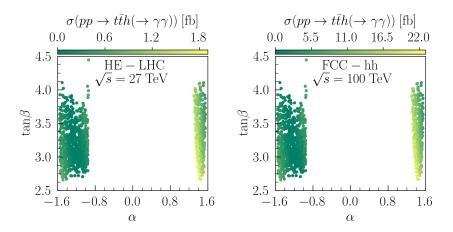


FIG. 6. The surviving samples are shown in the $\tan\beta$ versus α plane, with colors indicating the cross section of $pp \to t\bar{t}h(\to \gamma\gamma)$ at 27 TeV HE-LHC (left) and 100 TeV FCC-hh (right).

B. 27 TeV HE-LHC and 100 TeV FCC-hh Simulation Result

We also performed the same Monte Carlo simulations at the high-energy LHC (HE-LHC) [110] and the Future Circular Collider (FCC-hh) [111], which operate at collision energies of $\sqrt{s} = 27$ TeV and $\sqrt{s} = 100$ TeV, respectively. The integrated luminosity is set at L = 10 ab⁻¹ for the HE-LHC and L = 30 ab⁻¹ for the FCC-hh. We calculate the cross section $\sigma_{\text{HE-LHC(FCC-hh)}}$ for the process $pp \to t\bar{t}h(\to \gamma\gamma)$ at both the HE-LHC and the FCC-hh by

$$\sigma_{\text{HE-LHC(FCC-hh)}} = \sigma_{\text{HE-LHC(FCC-hh)}}^{\text{BP}} \times \frac{C_{t\bar{t}h}^2 \times Br(h \to \gamma\gamma)}{(C_{t\bar{t}h}^{\text{BP}})^2 \times Br^{\text{BP}}(h \to \gamma\gamma)},$$
(30)

where the cross section $\sigma_{\text{HE-LHC(FCC-hh)}}^{\text{BP}}$ for the Benchmark Point P1 at the 27 TeV HE-LHC and 100 TeV FCC-hh, calculated using MadGraph5_aMC@NLO_v3.4.2 [100, 101], corresponds to 1.77 fb and 21.3 fb, respectively. Additionally, $C_{t\bar{t}h}^{\text{BP}}$ and $Br^{\text{BP}}(h \to \gamma \gamma)$ denote the coupling and branching ratios for this benchmark point. Fig. 6 shows the cross sections for $pp \to t(\to W^+b)\bar{t}(\to W^-\bar{b})h(\to \gamma\gamma)$ at the HE-LHC (left) and the FCC-hh (right). It is observed that the surviving samples reach a cross section of about 1.9 fb at the HE-LHC and about 23 fb at the FCC-hh. The signal cross section shows a significant increase with higher collision energies.

The distributions of various kinematic variables for the signal and SM background at the 27 TeV HE-LHC and 100 TeV FCC-hh are similar to those at the HL-LHC, as shown in Fig. 4. In contrast to the HL-LHC simulations, the HE-LHC simulations include the

TABLE III. Cut flow of the cross sections at 27 TeV HE-LHC for benchmark point P1 with an integrated luminosity of L = 300 fb⁻¹, as detailed in Table I.

Cuts -	$\operatorname{Signal}(\sigma \times L)$	$\operatorname{Background}(\sigma \times L)$						
	$tar{t}h$	$tar{t}\gamma$	$t ar{t} H$	tjH	$bar{b}\gamma\gamma$	$t \bar t \gamma \gamma$	$tj\gamma\gamma$	$Wjj\gamma\gamma$
Initial	530	3168000	927	115	3408000	14178	19920	206009
Basic cut	38.45	6874.6	80.06	3.23	1192.8	776.6	358.5	995.0
Mass cut	25.26	0.0	0.111	0.002	68.16	17.22	5.13	12.36
Energy cut	23.75	0.0	0.111	0.002	0.0	16.27	3.21	10.3

TABLE IV. Cut flow of the cross sections at 100 TeV FCC-hh for benchmark point P1 with an integrated luminosity of L = 300 fb⁻¹, as detailed in Table I.

Cuts -	$\operatorname{Signal}(\sigma \times L)$	$\operatorname{Background}(\sigma \times L)$						
	$t ar{t} h$	$tar{t}\gamma$	$t \bar t H$	tjH	$b ar{b} \gamma \gamma$	$t\bar{t}\gamma\gamma$	$tj\gamma\gamma$	$Wjj\gamma\gamma$
Initial	6391	33120000	11724	1005	14856000	141570	138120	1255800
Basic cut	278.8	53985	621	17.1	6388.1	4764.2	1446.7	4897.6
Mass cut	178.5	662.4	1.06	0.0	148.6	91.0	24.82	37.67
Energy cut	166.3	0.0	0.821	0.0	0.0	78.86	21.28	25.12

following cuts:

• Basic Cut: We select events that include at least one lepton $(N(\ell) \ge 1)$, two photons $(N(\gamma) \ge 2)$, two jets $(N(j) \ge 2)$, and at least one b-jet $(N(b) \ge 1)$. For the transverse momentum (p_T) of jets, leptons, and photons, the following cuts are applied:

$$p_T[j_1] > 30 \text{ GeV}, \ p_T[\ell_1] > 20 \text{ GeV}, \ p_T[\gamma_1] > 30 \text{ GeV}.$$
 (31)

The spatial separation between jets and photons must meet the following criteria:

$$\Delta R[j_1, j_2] < 4, \ \Delta R[\gamma_1, \gamma_2] < 3.4.$$
 (32)

To further reduce the background from $t\bar{t}\gamma$, the pseudorapidity of the jet and lepton $(\eta_{j_1} \text{ and } \eta_{\ell_1})$ must meet the following criteria:

$$\eta_{j_1} > -3.4, \ \eta_{\ell_1} < 3.5.$$
(33)

• Mass Cut: For the invariant masses of the diphoton pair $(M[\gamma_1\gamma_2])$ and the diphoton with a b-jet $(M[\gamma_1\gamma_2b_1])$, we require:

93 GeV
$$< M[\gamma_1 \gamma_2] < 97$$
 GeV, $M[\gamma_1 \gamma_2 b_1] > 120$ GeV. (34)

For the transverse masses of the lepton, photon, diphoton, and diphoton with a b-jet $(M_T[\ell_1], M_T[\gamma_1], M_T[\gamma_1\gamma_2],$ and $M_T[\gamma_1\gamma_2b_1])$, we require:

$$M_T[\ell_1] < 40 \text{ GeV}, \ M_T[\gamma_1] < 380 \text{ GeV}, \ M_T[\gamma_1 \gamma_2 b] > 6 \text{ GeV}, \ M_T[\gamma_1 \gamma_2 b_1] < 500 \text{ GeV}.$$
(35)

• Energy Cut: The missing transverse energy $(\not\!E_T)$ is used to reduce the background of $Wjj\gamma\gamma$, which require

$$E_T > 15 \text{ GeV}.$$
 (36)

The cut flow for signal and background at the HE-LHC with an integrated luminosity of $L=300~{\rm fb^{-1}}$ is shown in Table III. The backgrounds of $t\bar{t}\gamma$, $b\bar{b}\gamma\gamma$ and $Wjj\gamma\gamma$ still play an important role. After the basic cut, the backgrounds of $t\bar{t}\gamma$ and $b\bar{b}\gamma\gamma$ are reduced by over two and three orders of magnitude, respectively. These backgrounds are further suppressed by subsequent cuts at the invariant mass and transverse mass. The $t\bar{t}\gamma$ background is nearly eliminated and no longer dominant. The $t\bar{t}H$ and tjH backgrounds become nearly negligible. Finally, the missing transverse energy cut effectively eliminates the $b\bar{b}\gamma\gamma$ background. However, the $t\bar{t}\gamma\gamma$, $tj\gamma\gamma$, and $Wjj\gamma\gamma$ backgrounds are difficult to remove and ultimately persist.

For the simulations at the FCC-hh, we implement the following cuts:

• Basic Cut: We select events containing at least one lepton $(N(\ell) \ge 1)$, two photons $(N(\gamma) \ge 2)$, two jets $(N(j) \ge 2)$, and at least one b-jet $(N(b) \ge 1)$. For the transverse momentum (p_T) of the jets and photons, we have the following requirements

$$p_T[\gamma_1] > 35 \text{ GeV}, \ p_T[j_2] < 220 \text{ GeV}, \ p_T[b_1] > 25 \text{ GeV}.$$
 (37)

The spatial separation between jets and photons must meet the following criteria:

$$\Delta R[j_1, j_2] < 4, \ \Delta R[\gamma_1, \gamma_2] < 3.4.$$
 (38)

To further reduce the background from $t\bar{t}\gamma$, we require that the phase angle of the lepton (θ_{ℓ_1}) and the pseudorapidity of the jet (η_{j_1}) meet the following criteria:

$$\theta_{\ell_1} > 0.1 \,, \ \eta_{j_1} > -3.8 \,.$$
 (39)

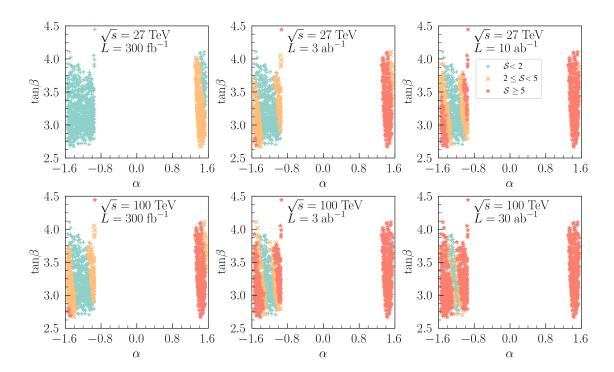


FIG. 7. Statistical significance of surviving samples in the $\tan \beta$ versus α planes at the 27 TeV HE-LHC for integrated luminosities of $L=300~{\rm fb^{-1}}$ (upper left), $L=3~{\rm ab^{-1}}$ (upper middle), and $L=10~{\rm ab^{-1}}$ (upper right); and at the 100 TeV FCC-hh for $L=300~{\rm fb^{-1}}$ (lower left), $L=3~{\rm ab^{-1}}$ (lower middle), and $L=30~{\rm ab^{-1}}$ (lower right).

• Mass Cut: For the invariant mass of the diphoton pair $M[\gamma_1\gamma_2]$, we choose the following criteria:

93 GeV
$$< M[\gamma_1 \gamma_2] < 97$$
 GeV. (40)

For the transverse mass of the photon and lepton, we apply the following criteria:

$$M_T[\gamma_1] < 330 \text{ GeV}, M_T[\ell_1] < 295 \text{ GeV}.$$
 (41)

• Energy Cut: The transverse hadronic energy (H_T) and the missing transverse energy (\cancel{E}_T) must meet the following criteria:

150 GeV
$$< H_T < 900$$
 GeV, $E_T > 10$ GeV. (42)

The cut flow of the cross sections for signal and background at the FCC-hh with an integrated luminosity of $L = 300 \text{ fb}^{-1}$ is shown in Table IV. As the collision energy increases

from 27 to 100 TeV, the cross sections for all signals and backgrounds, except for the $b\bar{b}\gamma\gamma$ background, increase about ten times. The primary backgrounds are $t\bar{t}\gamma$, $b\bar{b}\gamma\gamma$, and $Wjj\gamma\gamma$. The basic cut significantly reduces these backgrounds to a rare occurrence. After the basic cut, the backgrounds $b\bar{b}\gamma\gamma$, $t\bar{t}\gamma\gamma$, $tj\gamma\gamma$, and $Wjj\gamma\gamma$ become equally significant, each retaining a few thousand events. The resonance background tjH is almost eliminated by the diphoton invariant mass cut, and $t\bar{t}H$ is significantly reduced by the same cut. After the energy cut, both $t\bar{t}\gamma$ and $b\bar{b}\gamma\gamma$ are nearly eliminated. Finally, the remaining backgrounds include $t\bar{t}\gamma\gamma$, $tj\gamma\gamma$, $Wjj\gamma\gamma$, and a small amount of $t\bar{t}H$.

In Fig. 7, the statistical significance of the surviving samples is plotted for the 27 TeV HE-LHC (upper panel) and the 100 TeV FCC-hh (lower panel) at integrated luminosities of $L = 300 \text{ fb}^{-1}$ (left), $L = 3 \text{ ab}^{-1}$ (middle), and $L = 10 \text{ ab}^{-1}$ (right). The markers in the figure represent their respective statistical significance. We can draw several conclusions from these figures:

- Combining the left panel of Fig. 5 with the left two panels of Fig. 7, one can notice that for the same integrated luminosity, higher collider energies lead to greater statistical significance of the signal. This suggests that as the collision energy increases, less integrated luminosity is required to detect particles. For example, the FCC-hh at $L = 300 \text{ fb}^{-1}$ achieves a coverage comparable to the HL-LHC at $L = 1 \text{ ab}^{-1}$, and the FCC-hh at $L = 3 \text{ ab}^{-1}$ matches the coverage of the HE-LHC at $L = 10 \text{ ab}^{-1}$.
- For the benchmark point P1 at an integrated luminosity of $L = 300 \text{ fb}^{-1}$, we obtain a statistical significance of 3.9σ at the HE-LHC and 12.4σ at the FCC-hh. To achieve a statistical significance of 2σ or 5σ at the HE-LHC, a minimum of $L = 69 \text{ fb}^{-1}$ or $L = 430 \text{ fb}^{-1}$ is required. For the FCC-hh, these thresholds are significantly lower, at $L = 6.8 \text{ fb}^{-1}$ and $L = 42 \text{ fb}^{-1}$.
- From the upper middle and right panels of Fig. 7, all samples with $\alpha > 0$ reach coverage at 2σ or 5σ when L = 3 ab⁻¹, and all these samples reach 5σ significance when L = 10 ab⁻¹.
- From the lower left and middle panels of Fig. 7, it is evident that all samples within the region where $\alpha > 0$ achieve coverage at the 2σ level for the FCC-hh with an integrated luminosity of $L = 300 \text{ fb}^{-1}$, and reach the 5σ level with $L = 3 \text{ ab}^{-1}$.

• Even when the integrated luminosity is increased to 30 ab⁻¹, samples with $\alpha + \beta \approx 0$ are barely covered all at the 2σ level, as shown in the lower panel of Fig. 7. This is mainly because the light Higgs in this region has a very low branching ratio for $h \to \gamma \gamma$, making it difficult to detect by the diphoton decay process.

V. CONCLUSION

In this study, we explored the potential of the 2HDM-I to account for the 95 GeV diphoton excess observed at the LHC. By analyzing the dependence of Higgs boson couplings and decay branching ratios on the model parameters, we identified viable regions of parameter space consistent with current theoretical and experimental constraints.

We performed collider Monte Carlo simulations to evaluate the feasibility of discovering the 95 GeV Higgs boson at future colliders. Our analysis focused on the $pp \to t(\to W^+b)\bar{t}(\to W^-\bar{b})h(\to \gamma\gamma)$ process and its relevant backgrounds. Our simulations indicate that at the HL-LHC, statistical significances of 2σ and 5σ could be achieved at integrated luminosities of 137 fb⁻¹ and 859 fb⁻¹, respectively. Comparable levels of significance can be achieved at the HE-LHC and the FCC-hh with lower integrated luminosities, highlighting the advantages of higher-energy collisions.

Finally, we draw the following conclusions about the 95 GeV Higgs boson within the 2HDM-I:

- The analysis reveals that direct Higgs search data strongly constrain the model parameter α , excluding samples within the range $-0.9 \lesssim \alpha \lesssim 1.3$. Constraints from B-physics processes, particularly $B \to X_s \gamma$, require $\tan \beta \gtrsim 2.5$. Moreover, data on the muon anomalous magnetic moment (Δa_{μ}) exclude $|m_{12}|$ values that are either too small ($|m_{12}| \lesssim 20 \, m_A 500 \, \text{GeV}$) or too large ($|m_{12}| \gtrsim 20 \, m_A + 500 \, \text{GeV}$), as larger $|m_{12}|$ values contribute positively to Δa_{μ} .
- The branching ratio $Br(h \to \gamma \gamma)$ is primarily influenced by α and $\tan \beta$, reaching a maximum of 0.19 when $\sin \alpha$ approaches 1. The coupling ratio $C_{tth}/C_{tth}^{\rm SM}$ is nearly proportional to $\cos \alpha$, favoring larger values of $\cos \alpha$ for enhanced signals. The cross section $\sigma(pp \to t\bar{t}h(\to \gamma\gamma))$ peaks at approximately 0.6 fb when $\sin \alpha$ is near 1 and $\tan \beta$ is around 2.7.

- Collider simulations identify primary backgrounds, including $t\bar{t}\gamma$, $b\bar{b}\gamma\gamma$, and $Wjj\gamma\gamma$, with $t\bar{t}\gamma\gamma$, $tj\gamma\gamma$, and $Wjj\gamma\gamma$ proving particularly difficult to eliminate. Notably, even with increased collision energy or integrated luminosity, achieving comprehensive coverage of the parameter range $\alpha + \beta \approx 0$ at the 2σ level through the diphoton channel remains challenging. This is because h scarcely decays to diphotons within this parameter range.
- For the surviving samples, statistical significance of 2σ and 5σ can be achieved at the 14 TeV HL-LHC with integrated luminosities of $L=137~{\rm fb^{-1}}$ and $L=859~{\rm fb^{-1}}$, respectively. Comparable statistical significances can be achieved at the 27 TeV HE-LHC with integrated luminosities of $L=69~{\rm fb^{-1}}$ and $L=430~{\rm fb^{-1}}$, as well as at the 100 TeV FCC-hh with $L=6.8~{\rm fb^{-1}}$ and $L=42~{\rm fb^{-1}}$.

ACKNOWLEDGMENTS

This work was supported by the National Natural Science Foundation of China under Grant No. 12275066 and by the startup research funds of Henan University.

Note added. During the preparation of this manuscript, a paper with a comparable analysis was published on arXiv [10]. What's apart is that it starts from theory to explain experimental anomalies, whereas we place a greater emphasis on testing the model at future colliders.

^[1] S. Chatrchyan et al. (CMS), Phys. Lett. B **716**, 30 (2012), arXiv:1207.7235 [hep-ex].

^[2] G. Aad et al. (ATLAS), Phys. Lett. B 716, 1 (2012), arXiv:1207.7214 [hep-ex].

^[3] A. Tumasyan *et al.* (CMS), Nature **607**, 60 (2022), [Erratum: Nature 623, (2023)], arXiv:2207.00043 [hep-ex].

^[4] G. Aad *et al.* (ATLAS), Nature **607**, 52 (2022), [Erratum: Nature 612, E24 (2022)], arXiv:2207.00092 [hep-ex].

^[5] R. Barate et al. (LEP Working Group for Higgs boson searches, ALEPH, DELPHI, L3, OPAL), Phys. Lett. B 565, 61 (2003), arXiv:hep-ex/0306033.

^[6] A. M. Sirunyan et al. (CMS), Phys. Lett. B **793**, 320 (2019), arXiv:1811.08459 [hep-ex].

- [7] G. Aad et al. (ATLAS), CERN-EP-2024-166 (2024), arXiv:2407.07546 [hep-ex].
- [8] A. Hayrapetyan *et al.* (CMS), CMS-HIG-20-002, CERN-EP-2024-088 (2024), arXiv:2405.18149 [hep-ex].
- [9] D. Azevedo, T. Biekötter, and P. M. Ferreira, JHEP 11, 017 (2023), arXiv:2305.19716
 [hep-ph].
- [10] A. Khanna, S. Moretti, and A. Sarkar, (2024), arXiv:2409.02587 [hep-ph].
- [11] R. Benbrik, M. Boukidi, and S. Moretti, (2024), arXiv:2405.02899 [hep-ph].
- [12] A. Belyaev, R. Benbrik, M. Boukidi, M. Chakraborti, S. Moretti, and S. Semlali, JHEP 05, 209 (2024), arXiv:2306.09029 [hep-ph].
- [13] R. Benbrik, M. Boukidi, S. Moretti, and S. Semlali, Phys. Lett. B 832, 137245 (2022), arXiv:2204.07470 [hep-ph].
- [14] S. Ashanujjaman, S. Banik, G. Coloretti, A. Crivellin, B. Mellado, and A.-T. Mulaudzi, Phys. Rev. D 108, L091704 (2023), arXiv:2306.15722 [hep-ph].
- [15] Z.-f. Ge, F.-Y. Niu, and J.-L. Yang, Eur. Phys. J. C 84, 548 (2024), arXiv:2405.07243
 [hep-ph].
- [16] A. Ahriche, M. L. Bellilet, M. O. Khojali, M. Kumar, and A.-T. Mulaudzi, Phys. Rev. D 110, 015025 (2024), arXiv:2311.08297 [hep-ph].
- [17] P. S. B. Dev, R. N. Mohapatra, and Y. Zhang, Phys. Lett. B 849, 138481 (2024), arXiv:2312.17733 [hep-ph].
- [18] A. Kundu, S. Maharana, and P. Mondal, Nucl. Phys. B 955, 115057 (2020), arXiv:1907.12808 [hep-ph].
- [19] J. A. Aguilar-Saavedra and F. R. Joaquim, Eur. Phys. J. C 80, 403 (2020), arXiv:2002.07697 [hep-ph].
- [20] S. Yaser Ayazi, M. Hosseini, S. Paktinat Mehdiabadi, and R. Rouzbehi, Phys. Rev. D 110, 055004 (2024), arXiv:2405.01132 [hep-ph].
- [21] L. Liu, H. Qiao, K. Wang, and J. Zhu, Chin. Phys. C 43, 023104 (2019), arXiv:1812.00107 [hep-ph].
- [22] K. Wang and J. Zhu, Chin. Phys. C 48, 073105 (2024), arXiv:2402.11232 [hep-ph].
- [23] S. Heinemeyer, C. Li, F. Lika, G. Moortgat-Pick, and S. Paasch, Phys. Rev. D 106, 075003 (2022), arXiv:2112.11958 [hep-ph].
- [24] T. Biekötter and M. O. Olea-Romacho, JHEP 10, 215 (2021), arXiv:2108.10864 [hep-ph].

- [25] T. Biekötter, S. Heinemeyer, and G. Weiglein, Phys. Lett. B 846, 138217 (2023), arXiv:2303.12018 [hep-ph].
- [26] T. Biekötter, S. Heinemeyer, and G. Weiglein, Phys. Rev. D 109, 035005 (2024), arXiv:2306.03889 [hep-ph].
- [27] G. Arcadi, G. Busoni, D. Cabo-Almeida, and N. Krishnan, (2023), arXiv:2311.14486 [hep-ph].
- [28] T. Biekötter, M. Chakraborti, and S. Heinemeyer, Eur. Phys. J. C 80, 2 (2020), arXiv:1903.11661 [hep-ph].
- [29] T. Biekötter, A. Grohsjean, S. Heinemeyer, C. Schwanenberger, and G. Weiglein, Eur. Phys. J. C 82, 178 (2022), arXiv:2109.01128 [hep-ph].
- [30] S. Banik, A. Crivellin, S. Iguro, and T. Kitahara, Phys. Rev. D 108, 075011 (2023), arXiv:2303.11351 [hep-ph].
- [31] J. A. Aguilar-Saavedra, H. B. Câmara, F. R. Joaquim, and J. F. Seabra, Phys. Rev. D 108, 075020 (2023), arXiv:2307.03768 [hep-ph].
- [32] C. Wang, J.-Q. Tao, M. A. Shahzad, G.-M. Chen, and S. Gascon-Shotkin, Chin. Phys. C 46, 083107 (2022), arXiv:2204.09198 [hep-ph].
- [33] T.-K. Chen, C.-W. Chiang, S. Heinemeyer, and G. Weiglein, Phys. Rev. D 109, 075043 (2024), arXiv:2312.13239 [hep-ph].
- [34] A. Ahriche, Phys. Rev. D 110, 035010 (2024), arXiv:2312.10484 [hep-ph].
- [35] J. Cao, X. Guo, Y. He, P. Wu, and Y. Zhang, Phys. Rev. D 95, 116001 (2017), arXiv:1612.08522 [hep-ph].
- [36] J. Cao, X. Jia, Y. Yue, H. Zhou, and P. Zhu, Phys. Rev. D 101, 055008 (2020), arXiv:1908.07206 [hep-ph].
- [37] W. G. Hollik, C. Li, G. Moortgat-Pick, and S. Paasch, Eur. Phys. J. C 81, 141 (2021), arXiv:2004.14852 [hep-ph].
- [38] W. Li, H. Qiao, and J. Zhu, Chin. Phys. C 47, 123102 (2023), arXiv:2212.11739 [hep-ph].
- [39] F. Domingo, U. Ellwanger, and C. Hugonie, Eur. Phys. J. C 82, 1074 (2022), arXiv:2209.03863 [hep-ph].
- [40] J. Cao, X. Jia, J. Lian, and L. Meng, Phys. Rev. D 109, 075001 (2024), arXiv:2310.08436 [hep-ph].
- [41] W. Li, H. Qiao, K. Wang, and J. Zhu, (2023), arXiv:2312.17599 [hep-ph].

- [42] J. Lian, (2024), arXiv:2406.10969 [hep-ph].
- [43] J. Cao, X. Jia, and J. Lian, (2024), arXiv:2402.15847 [hep-ph].
- [44] U. Ellwanger and C. Hugonie, Eur. Phys. J. C 83, 1138 (2023), arXiv:2309.07838 [hep-ph].
- [45] U. Ellwanger, C. Hugonie, S. F. King, and S. Moretti, Eur. Phys. J. C 84, 788 (2024), arXiv:2404.19338 [hep-ph].
- [46] K. Wang, F. Wang, J. Zhu, and Q. Jie, Chin. Phys. C 42, 103109 (2018), arXiv:1811.04435
 [hep-ph].
- [47] T. D. Lee, Phys. Rev. D 8, 1226 (1973).
- [48] G. C. Branco, P. M. Ferreira, L. Lavoura, M. N. Rebelo, M. Sher, and J. P. Silva, Phys. Rept. 516, 1 (2012), arXiv:1106.0034 [hep-ph].
- [49] D. Atwood, L. Reina, and A. Soni, Phys. Rev. D 55, 3156 (1997), arXiv:hep-ph/9609279.
- [50] J. F. Gunion and H. E. Haber, Phys. Rev. D 67, 075019 (2003), arXiv:hep-ph/0207010.
- [51] G. Bhattacharyya and D. Das, Pramana 87, 40 (2016), arXiv:1507.06424 [hep-ph].
- [52] L. Wang, J. M. Yang, and Y. Zhang, Commun. Theor. Phys. 74, 097202 (2022), arXiv:2203.07244 [hep-ph].
- [53] H. E. Haber and G. L. Kane, Phys. Rept. 117, 75 (1985).
- [54] A. Pich and P. Tuzon, Phys. Rev. D 80, 091702 (2009), arXiv:0908.1554 [hep-ph].
- [55] P. Tuzon and A. Pich, Acta Phys. Polon. Supp. 3, 215 (2010), arXiv:1001.0293 [hep-ph].
- [56] H. E. Haber, G. L. Kane, and T. Sterling, Nucl. Phys. B 161, 493 (1979).
- [57] L. J. Hall and M. B. Wise, Nucl. Phys. B **187**, 397 (1981).
- [58] A. Arhrib, R. Benbrik, R. Enberg, W. Klemm, S. Moretti, and S. Munir, Phys. Lett. B 774, 591 (2017), arXiv:1706.01964 [hep-ph].
- [59] Y. Wang, A. Arhrib, R. Benbrik, M. Krab, B. Manaut, S. Moretti, and Q.-S. Yan, JHEP12, 021 (2021), arXiv:2107.01451 [hep-ph].
- [60] P. Posch, Phys. Lett. B **696**, 447 (2011), arXiv:1001.1759 [hep-ph].
- [61] G. Aad et al. (ATLAS), JHEP 06, 097 (2022), arXiv:2111.06712 [hep-ex].
- [62] G. Aad et al. (ATLAS), (2024), arXiv:2407.10904 [hep-ex].
- [63] M. Aoki, S. Kanemura, K. Tsumura, and K. Yagyu, Phys. Rev. D 80, 015017 (2009), arXiv:0902.4665 [hep-ph].
- [64] M. Carena and H. E. Haber, Prog. Part. Nucl. Phys. 50, 63 (2003), arXiv:hep-ph/0208209.
- [65] A. Djouadi, Phys. Rept. **459**, 1 (2008), arXiv:hep-ph/0503173.

- [66] Y. Bai, V. Barger, L. L. Everett, and G. Shaughnessy, Phys. Rev. D 87, 115013 (2013), arXiv:1210.4922 [hep-ph].
- [67] F. Staub, Comput. Phys. Commun. 181, 1077 (2010), arXiv:0909.2863 [hep-ph].
- [68] F. Staub, Comput. Phys. Commun. **182**, 808 (2011), arXiv:1002.0840 [hep-ph].
- [69] F. Staub, Comput. Phys. Commun. 184, 1792 (2013), arXiv:1207.0906 [hep-ph].
- [70] F. Staub, Comput. Phys. Commun. 185, 1773 (2014), arXiv:1309.7223 [hep-ph].
- [71] W. Porod, Comput. Phys. Commun. 153, 275 (2003), arXiv:hep-ph/0301101.
- [72] W. Porod and F. Staub, Comput. Phys. Commun. 183, 2458 (2012), arXiv:1104.1573 [hep-ph].
- [73] M. Aaboud et al. (ATLAS), JHEP **04**, 098 (2019), arXiv:1812.03017 [hep-ex].
- [74] A. M. Sirunyan et al. (CMS), JHEP 04, 188 (2020), arXiv:1910.12127 [hep-ex].
- [75] R. Aaij et al. (LHCb), Phys. Rev. Lett. **128**, 041801 (2022), arXiv:2108.09284 [hep-ex].
- [76] Y. S. Amhis et al. (HFLAV), Phys. Rev. D 107, 052008 (2023), arXiv:2206.07501 [hep-ex].
- [77] R. L. Workman et al. (Particle Data Group), PTEP 2022, 083C01 (2022).
- [78] F. Mahmoudi, Comput. Phys. Commun. 178, 745 (2008), arXiv:0710.2067 [hep-ph].
- [79] F. Mahmoudi, Comput. Phys. Commun. 180, 1579 (2009), arXiv:0808.3144 [hep-ph].
- [80] D. P. Aguillard et al. (Muon g-2), Phys. Rev. Lett. 131, 161802 (2023), arXiv:2308.06230 [hep-ex].
- [81] S. Navas et al. (Particle Data Group), Phys. Rev. D 110, 030001 (2024).
- [82] P. Athron, M. Bach, H. G. Fargnoli, C. Gnendiger, R. Greifenhagen, J.-h. Park, S. Paßehr, D. Stöckinger, H. Stöckinger-Kim, and A. Voigt, Eur. Phys. J. C 76, 62 (2016), arXiv:1510.08071 [hep-ph].
- [83] P. Athron, C. Balazs, A. Cherchiglia, D. H. J. Jacob, D. Stöckinger, H. Stöckinger-Kim, and A. Voigt, Eur. Phys. J. C 82, 229 (2022), arXiv:2110.13238 [hep-ph].
- [84] P. Bechtle, D. Dercks, S. Heinemeyer, T. Klingl, T. Stefaniak, G. Weiglein, and J. Wittbrodt, Eur. Phys. J. C 80, 1211 (2020), arXiv:2006.06007 [hep-ph].
- [85] P. Bechtle, S. Heinemeyer, T. Klingl, T. Stefaniak, G. Weiglein, and J. Wittbrodt, Eur. Phys. J. C 81, 145 (2021), arXiv:2012.09197 [hep-ph].
- [86] M. E. Peskin and T. Takeuchi, Phys. Rev. Lett. 65, 964 (1990).
- [87] M. E. Peskin and T. Takeuchi, Phys. Rev. D 46, 381 (1992).
- [88] S. Kanemura, T. Kubota, and E. Takasugi, Phys. Lett. B 313, 155 (1993), arXiv:hep-

- ph/9303263.
- [89] A. G. Akeroyd, A. Arhrib, and E.-M. Naimi, Phys. Lett. B 490, 119 (2000), arXiv:hep-ph/0006035.
- [90] A. Arhrib, in Workshop on Noncommutative Geometry, Superstrings and Particle Physics (2000) arXiv:hep-ph/0012353.
- [91] A. W. El Kaffas, W. Khater, O. M. Ogreid, and P. Osland, Nucl. Phys. B 775, 45 (2007), arXiv:hep-ph/0605142.
- [92] Y.-F. Zhou and Y.-L. Wu, Eur. Phys. J. C 27, 577 (2003), arXiv:hep-ph/0110302.
- [93] K. A. Assamagan, A. Deandrea, and P.-A. Delsart, Phys. Rev. D 67, 035001 (2003), arXiv:hep-ph/0207302.
- [94] S. Davidson and G. J. Grenier, Phys. Rev. D 81, 095016 (2010), arXiv:1001.0434 [hep-ph].
- [95] X.-F. Han, F. Wang, L. Wang, J. M. Yang, and Y. Zhang, Chin. Phys. C 46, 103105 (2022), arXiv:2204.06505 [hep-ph].
- [96] A. Cherchiglia, P. Kneschke, D. Stöckinger, and H. Stöckinger-Kim, JHEP 01, 007 (2017),
 [Erratum: JHEP 10, 242 (2021)], arXiv:1607.06292 [hep-ph].
- [97] A. Cherchiglia, D. Stöckinger, and H. Stöckinger-Kim, Phys. Rev. D 98, 035001 (2018), arXiv:1711.11567 [hep-ph].
- [98] S.-P. Li, X.-Q. Li, Y.-Y. Li, Y.-D. Yang, and X. Zhang, JHEP **01**, 034 (2021), arXiv:2010.02799 [hep-ph].
- [99] S. Dittmaier et al. (LHC Higgs Cross Section Working Group), CERN-2011-002 (2011), 10.5170/CERN-2011-002, arXiv:1101.0593 [hep-ph].
- [100] J. Alwall, M. Herquet, F. Maltoni, O. Mattelaer, and T. Stelzer, JHEP 06, 128 (2011), arXiv:1106.0522 [hep-ph].
- [101] J. Alwall, R. Frederix, S. Frixione, V. Hirschi, F. Maltoni, O. Mattelaer, H. S. Shao, T. Stelzer, P. Torrielli, and M. Zaro, JHEP 07, 079 (2014), arXiv:1405.0301 [hep-ph].
- [102] R. D. Ball et al. (NNPDF), JHEP **04**, 040 (2015), arXiv:1410.8849 [hep-ph].
- [103] A. Buckley, J. Ferrando, S. Lloyd, K. Nordström, B. Page, M. Rüfenacht, M. Schönherr, and G. Watt, Eur. Phys. J. C 75, 132 (2015), arXiv:1412.7420 [hep-ph].
- [104] T. Sjöstrand, S. Ask, J. R. Christiansen, R. Corke, N. Desai, P. Ilten, S. Mrenna, S. Prestel, C. O. Rasmussen, and P. Z. Skands, Comput. Phys. Commun. 191, 159 (2015), arXiv:1410.3012 [hep-ph].

- [105] M. Cacciari, G. P. Salam, and G. Soyez, JHEP 04, 063 (2008), arXiv:0802.1189 [hep-ph].
- [106] J. de Favereau, C. Delaere, P. Demin, A. Giammanco, V. Lemaître, A. Mertens, and M. Selvaggi (DELPHES 3), JHEP **02**, 057 (2014), arXiv:1307.6346 [hep-ex].
- [107] M. Selvaggi, J. Phys. Conf. Ser. **523**, 012033 (2014).
- [108] E. Conte, B. Fuks, and G. Serret, Comput. Phys. Commun. 184, 222 (2013), arXiv:1206.1599
 [hep-ph].
- [109] G. Cowan, K. Cranmer, E. Gross, and O. Vitells, Eur. Phys. J. C 71, 1554 (2011), [Erratum: Eur.Phys.J.C 73, 2501 (2013)], arXiv:1007.1727 [physics.data-an].
- [110] M. Cepeda et al., CERN Yellow Rep. Monogr. 7, 221 (2019), arXiv:1902.00134 [hep-ph].
- [111] A. Abada et al. (FCC), Eur. Phys. J. ST 228, 755 (2019).